ISSN 1029-9599, Physical Mesomechanics, 2023, Vol. 26, No. 6, pp. 666–677. © Pleiades Publishing, Ltd., 2023.
Russian Text © The Author(s), 2023, published in Fizicheskaya Mezomekhanika, 2023, Vol. 26, No. 4, pp. 90–102.

A Study of the Structure and Mechanical Properties of Nb-Mo-Co-X (X = Hf, Zr, Ti) Refractory High-Entropy Alloys

E. S. Panina[1]*, N. Yu. Yurchenko[1], A. A. Tozhibaev[1], M. V. Mishunin[1], S. V. Zherebtsov[1], and N. D. Stepanov[1]

[1] *Belgorod State University, Belgorod, 308015 Russia*
** e-mail: panina_e@bsu.edu.ru*

Received October 3, 2022; revised January 10, 2023; accepted January 11, 2023

Abstract—Refractory high-entropy alloys (HEAs) are a new class of metallic materials based on group 4–6 elements of the periodic table with possible additions of Al, Si, Re, C, or B. Some single-phase refractory HEAs can maintain high strength up to 1600°C, while multiphase compositions have more attractive specific properties at temperatures up to 1200°C. Here we examine the structure and mechanical properties of refractory HEAs $Nb_{30}Mo_{30}Co_{20}Hf_{20}$, $Nb_{30}Mo_{30}Co_{20}Zr_{20}$, and $Nb_{30}Mo_{30}Co_{20}Ti_{20}$ (at %). The alloys consisted of an intermetallic B2 matrix and particles of a disordered bcc phase, as well as a minor volume fraction of additional bcc ($Nb_{30}Mo_{30}Co_{20}Hf_{20}$ and $Nb_{30}Mo_{30}Co_{20}Zr_{20}$) or fcc ($Nb_{30}Mo_{30}Co_{20}Ti_{20}$) phases. When tested for uniaxial compression, $Nb_{30}Mo_{30}Co_{20}Ti_{20}$ alloy showed a higher yield strength in the temperature range of 22–1000°C than $Nb_{30}Mo_{30}Co_{20}Hf_{20}$ and $Nb_{30}Mo_{30}Co_{20}Zr_{20}$ alloys. $Nb_{30}Mo_{30}Co_{20}Zr_{20}$ alloy did not fail at temperatures of 22–800°C to a given 50% strain, while $Nb_{30}Mo_{30}Co_{20}Ti_{20}$ alloy turned out to be brittle. All alloys demonstrated high strain hardening in the temperature range of 22–800°C, and they can compete in terms of specific strength with commercial nickel and cobalt superalloys.

Keywords: refractory high-entropy alloys, structure, mechanical properties

DOI: 10.1134/S1029959923060061

1. INTRODUCTION

Advances in the aerospace and energy industries require the development of new materials with higher performance characteristics. In the past few decades, nickel-based superalloys have been the most popular alloys in the aviation industry [1, 2]. Being composed of the ductile parent γ (fcc) phase and strong γ′ (L12) particles [3–8], these alloys demonstrate balanced properties up to 1150°C. However, the turbine inlet temperature in modern aircraft engines approaches 1700°C, which requires the use of thermal barrier coatings and additional cooling, which significantly reduces the engine efficiency [9].

Materials consisting of three or more components with the concentration 5–35 at % each [10], referred to as medium/high entropy alloys [11–14], are now being extensively investigated. This research field is a promising alternative for increasing the operating temperatures of moving parts of gas turbine engines. In particular, high-entropy alloys based on refractory elements demonstrate attractive strength at temperatures up to 1600°C [15–17]. Refractory high-entropy alloys have a predominantly single-phase bcc structure, which complicates the control over their mechanical properties [16, 18, 19]. However, it is known from experience that the introduction of reinforcing particles into the soft matrix of nickel superalloys increases their strength without loss of ductility [20]. This approach was used to develop refractory high-entropy superalloys with a two-phase bcc-B2 structure (ordered binary B2 compounds with a bcc lattice, a CsCl-type structure) [21–26]. However, these alloys often proved to be unstable at temperatures above 700°C. Brittle intermetallic compounds formed in the alloy, causing the material embrittlement [27–29].

A more stable bcc-B2 structure can be formed in refractory alloys, including high-entropy ones, by using B2 compounds based on group 4 and 8–10 elements of the periodic table. In particular, W-Ti-Fe alloys can exhibit high strength at $T = 1000°C$ due to semicoherent Ti- and Fe-rich B2 particles [30]. It was reported in [31] that the B2 phase can also be used as a ductile matrix. The authors proposed a Nb30Mo30Co20Hf20 alloy (at %), which had balanced mechanical properties at $T < 1000°C$ and exceptional capacity for strain hardening at 22–600°C. The soft Hf- and Co-rich B2 matrix contributed to blunting of cracks formed in hard (Nb, Mo)-rich bcc particles, which made the strain hardening stage longer and increased the ductility.

Apart from HfCo, there are two more B2 compounds with high ductility even under tension [32, 33], namely, ZrCo and TiCo, which show promise for the development of lighter high-temperature composites. This paper compares the results of the microstructural and mechanical investigations as well as of microhardness measurements of the phases of the alloys $Nb_{30}Mo_{30}Co_{20}Hf_{20}$, $Nb_{30}Mo_{30}Co_{20}Ti_{20}$, and $Nb_{30}Mo_{30}Co_{20}Zr_{20}$.

2. MATERIALS AND METHODS OF INVESTIGATION

The investigation is concerned with the composites $Nb_{30}Mo_{30}Co_{20}Hf_{20}$, $Nb_{30}Mo_{30}Co_{20}Ti_{20}$, and $Nb_{30}Mo_{30}Co_{20}Zr_{20}$ (at %). These alloys were obtained by vacuum-arc remelting of high-purity metals (no less than 99.9 wt %) in the copper mold under an argon atmosphere. Pure metals had the form of cylindrical granules 2.4 mm in diameter and 3.0 mm in height. The chemical composition of the alloys is presented in Table 1. The ingot measured $\approx 7 \times 11 \times 55\ mm^3$.

Phase diagrams and phase compositions of the alloys $Nb_{30}Mo_{30}Co_{20}Hf_{20}$, $Nb_{30}Mo_{30}Co_{20}Zr_{20}$, and $Nb_{30}Mo_{30}Co_{20}Ti_{20}$ were modeled using Thermo-Calc software (version 2022a) with TCHEA4 databases. The microstructure of the alloys was studied using backscattered electron scanning microscopy (SEM), transmission electron microscopy (TEM), and scanning transmission electron microscopy (STEM). SEM studies were carried out under FEI Quanta 600 FEG microscopes. TEM studies were performed under a JEOL JEM-2100 microscope equipped with the energy dispersive detector. The volume fraction was measured manually according to GOST R ISO 9042-2011 using a point grid. The method consists in applying a point grid to a given number of fields of the studied surface, counting the number of grid points within the structural component, and then calculating its volume fraction. The volume fraction is calculated using the formula

$$Vv = \overline{P}p = \frac{1}{n}\sum_{i=1}^{n} Pp(i), \tag{1}$$

where n is the number of the studied fields, $\overline{P}p$ is the arithmetic mean of $Pp(i)$, $Pp(i) = P_i/P_t$ is the fraction of grid points within the considered structural component in the ith field, P_i is the number of points in the ith field, and P_t is the total number of grid points. Mechanical compression tests on rectangular specimens with the dimensions $5 \times 3 \times 3\ mm^3$ were carried out in air at 22, 600, 800 and 1000°C on an Instron 300LX testing machine equipped with the radial furnace. Before testing at 600–1000°C, the specimens were placed into the preheated furnace and held for 10 min to attain the test temperature. The specimen temperature was controlled by the thermocouple attached to the side surface of a specimen. The initial strain rate was $10^{-4}\ s^{-1}$. The stress is calculated by the formula

$$\sigma = F/S, \tag{2}$$

where F is the load applied to the specimen, and S is the initial cross-sectional area of the specimen.

Strain hardening is calculated using the formula

$$\frac{\Delta\sigma}{\Delta\varepsilon} = \frac{\sigma_{0.05} - \sigma_{0.002}}{0.05 - 0.002}, \tag{3}$$

where $\sigma_{0.05}$ is the stress at the true strain 0.05, and $\sigma_{0.002}$ is the yield strength [31]. Hardness measurements were carried out using a Shimadzu DUH-211s dynamic ultramicrohardness tester equipped with the Berkovich indenter. At least twenty indentations were performed for each of the phases, avoiding any influence of the adjacent phase(s). The maximum load was 50 mN with the loading time 5 s and rate 6.6620 mN/s. The hardness and elastic modulus were obtained using the method described in [27].

Table 1. Chemical composition of the alloys $Nb_{30}Mo_{30}Co_{20}Hf_{20}$, $Nb_{30}Mo_{30}Co_{20}Ti_{20}$, and $Nb_{30}Mo_{30}Co_{20}Zr_{20}$

Alloy	Density, g/cm^3	Element, at %							
		Nb	Mo	Co	Hf	Zr	Ti	O, g/t	N, g/t
$Nb_{30}Mo_{30}Co_{20}Hf_{20}$	10.4 ± 0.2	28.2 ± 0.8	30.3 ± 0.5	20.9 ± 0.4	20.7 ± 0.3	–	–	390 ± 15	30 ± 2
$Nb_{30}Mo_{30}Co_{20}Zr_{20}$	8.5 ± 0.3	29.6 ± 0.3	30.8 ± 0.6	20.1 ± 0.3	–	19.5 ± 0.4	–	434 ± 15	39 ± 4
$Nb_{30}Mo_{30}Co_{20}Ti_{20}$	8.2 ± 0.1	28.8 ± 0.4	32.8 ± 0.3	19.4 ± 0.2	–	–	19.0 ± 0.5	392 ± 12	49 ± 5

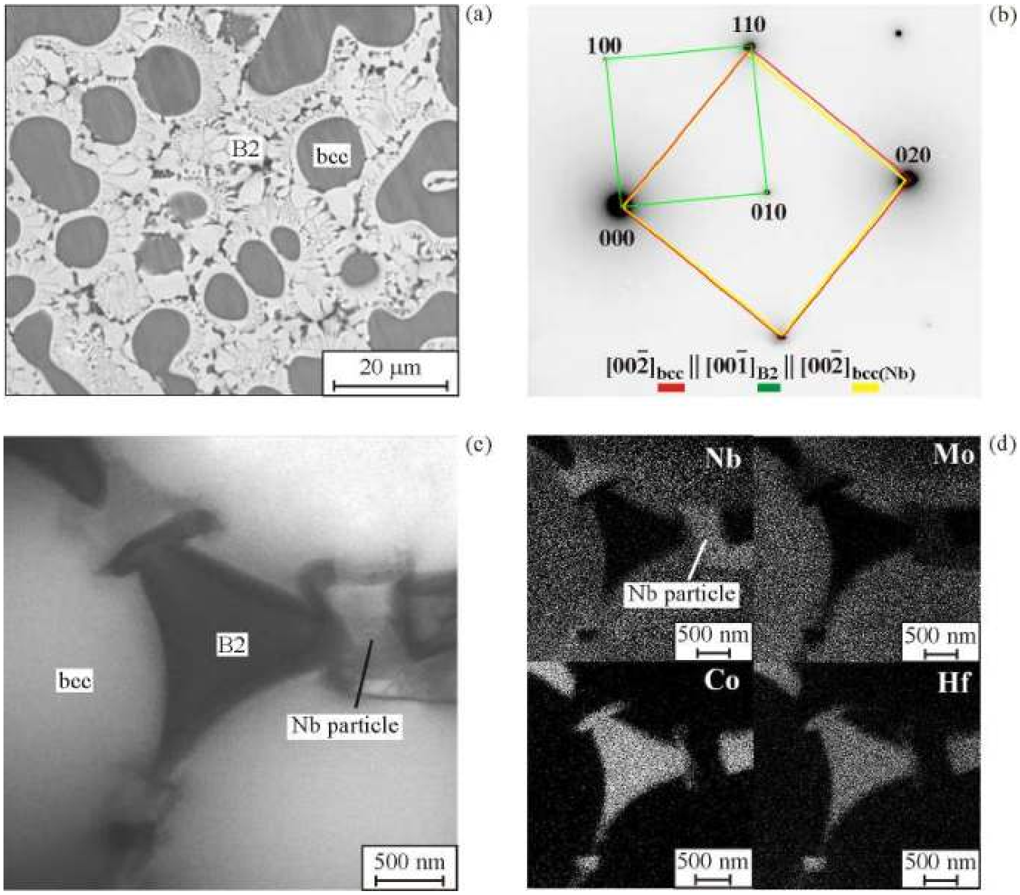

Fig. 1. Microstructure of the $Nb_{30}Mo_{30}Co_{20}Hf_{20}$ alloy: SEM image (a); SAED pattern demonstrating the orientation relationships: $(110)_{bcc} \,||\, (110)_{B2} \,||\, (110)_{bcc(Nb)}$, $[00\bar{2}]_{bcc} \,||\, [00\bar{1}]_{B2} \,||\, [00\bar{2}]_{bcc(Nb)}$ (b); STEM image (c); element distribution maps (d) (color online).

3. RESULTS

3.1. Microstructure

The structural-phase investigation of the $Nb_{30}Mo_{30}Co_{20}Hf_{20}$ alloy shows the presence of three components (Fig. 1a). The Hf- and Co-rich B2 matrix (the light phase in Fig. 1a) contains ellipsoidal Nb- and Mo-rich bcc particles (the dark gray phase in Fig. 1a). Rare small Nb-rich particles are also found at the bcc-B2 phase boundaries (Figs. 1a, 1b, Table 2). The orientations of the three phases are in the

Table 2. Chemical composition of structural components of the alloys $Nb_{30}Mo_{30}Co_{20}Hf_{20}$, $Nb_{30}Mo_{30}Co_{20}Zr_{20}$, and $Nb_{30}Mo_{30}Co_{20}Ti_{20}$

Alloy	Phase	Volume fraction, %	Element, at %					
			Nb	Mo	Co	Hf	Zr	Ti
$Nb_{30}Mo_{30}Co_{20}Hf_{20}$	B2	47.4 ± 0.5	7.3 ± 0.2	3.3 ± 0.5	45.4 ± 1.3	44.0 ± 0.8	–	–
	bcc	51.1 ± 0.8	36.0 ± 0.3	53.5 ± 0.8	2.1 ± 0.2	8.4 ± 0.6	–	–
	Nb particles	1.5 ± 0.3	57.4 ± 0.5	26.9 ± 1.1	7.9 ± 0.5	7.8 ± 0.3	–	–
$Nb_{30}Mo_{30}Co_{20}Zr_{20}$	B2	39.0 ± 0.9	7.3 ± 0.6	4.0 ± 0.7	44.3 ± 0.6	–	44.4 ± 0.8	–
	bcc	60.0 ± 1.1	46.4 ± 0.4	44.8 ± 1.1	3.3 ± 0.4	–	5.5 ± 0.7	–
	Nb particles	1.0 ± 0.4	73.8 ± 0.5	19.0 ± 0.3	1.4 ± 0.2	–	5.8 ± 0.3	–
$Nb_{30}Mo_{30}Co_{20}Ti_{20}$	B2	29.0 ± 1.5	14.1 ± 0.2	4.5 ± 0.3	45.9 ± 0.8	–	–	35.6 ± 0.6
	bcc	70.0 ± 1.2	37.9 ± 0.5	48.6 ± 0.8	2.7 ± 0.3	–	–	10.8 ± 0.4
	Ti particles	1.0 ± 0.2	3.9 ± 0.3	0.5 ± 0.2	0.5 ± 0.2	–	–	95.1 ± 1.1

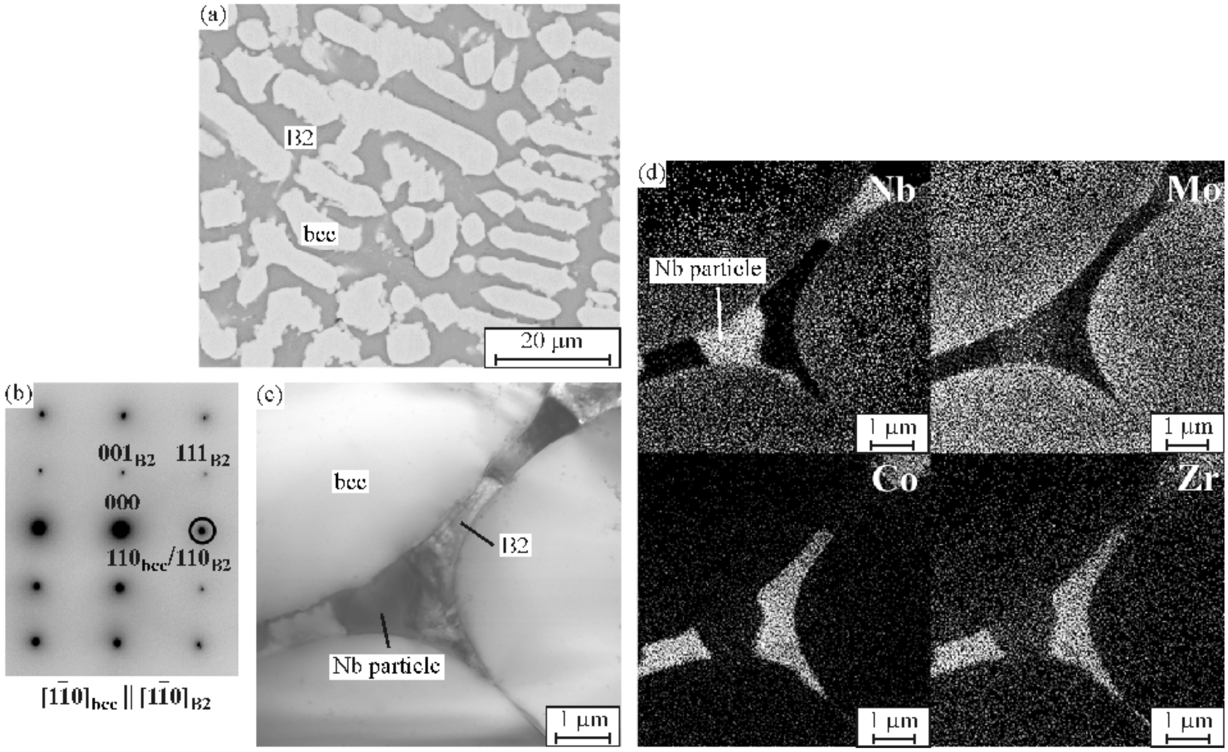

Fig. 2. Microstructure of the $Nb_{30}Mo_{30}Co_{20}Zr_{20}$ alloy: SEM image showing the composite structure including the bcc and B2 phases (a); SAED pattern demonstrating the cube-on-cube orientation relationship: $(110)_{bcc} \| (110)_{B2}$, $[0\bar{1}0]_{bcc} \| [0\bar{1}0]_{B2}$ (b); STEM image (c); element distribution maps (d).

ratio: $(110)_{bcc} \| (110)_{B2} \| (110)_{bcc(Nb)}$, $[001]_{bcc} \| [001]_{B2} \| [001]_{bcc(Nb)}$ (Fig. 1c). This cube-on-cube orientation relationship is typical for alloys with a bcc-B2 structure [23, 25, 30, 31, 34]. The volume fractions of the B2, bcc(Nb, Mo) (niobium- and molybdenum-rich) and bcc(Nb) (niobium-rich) phases are ≈47, ≈51, and <2%, respectively (Table 2).

The $Nb_{30}Mo_{30}Co_{20}Zr_{20}$ alloy consists of a Zr- and Co-rich B2 matrix (the dark gray phase in Fig. 2a) and a Nb- and Mo-rich bcc phase (the light phase in Fig. 2a) (Figs. 2a, 2b, Table 2). In the zirconium alloy, the bcc particles have a more elongated shape than those in the $Nb_{30}Mo_{30}Co_{20}Hf_{20}$ alloy (Figs. 1a, 2a). The detailed study of the alloy reveals a small amount of the Nb-rich bcc phase (Figs. 2c, 2d, Table 2) at the bcc-B2 phase boundaries, as in the $Nb_{30}Mo_{30}Co_{20}Hf_{20}$ alloy (Fig. 1). A cube-on-cube orientation relationship is also found between the structural components (Fig. 2b). The volume fraction of the B2, (Nb, Mo)-rich bcc and Nb-rich bcc phases is ≈39, ≈60, and ≈1%, respectively (Table 2).

The typical structural-phase state of the $Nb_{30}Mo_{30}Co_{20}Ti_{20}$ alloy is represented by two dominant phases: islands of the bcc phase (the light phase in Fig. 3a) located in the parent B2 phase (the dark gray phase in Fig. 3a). In this case, the bcc phase is enriched in niobium and molybdenum, and the B2 phase is enriched in cobalt and titanium (Figs. 3a, 3c, 3d, Table 2). A Ti- and O-rich phase (40.1% O–36.4% Ti–16.6% Co–5.9% Nb–1.0% Mo) with an fcc structure was also detected (Figs. 3b–3d, Table 2). Particles of the fcc phase are located within the B2 phase, as well as near the bcc-B2 phase boundaries. The volume fractions of the bcc, B2, and fcc phases are ≈70, ≈29, and <1%, respectively (Table 2).

3.2. Mechanical Properties

The $Nb_{30}Mo_{30}Co_{20}Hf_{20}$ alloy shows high strength and sufficient strain to fracture both at room temperature and at 1000°C (Fig. 4, Table 3). In particular, the yield strength and fracture strain at 22°C are equal to 1180 MPa and 10%, respectively. At 1000°C, the yield strength remains at the level 370 MPa, and the ductility increases to >40%. A substitution of Zr for Hf gives a considerable increase in ductility (by more than 4 times at 22°C) (Fig. 4, Table 3). However, at higher temperature, the ductility of the alloys $Nb_{30}Mo_{30}Co_{20}Hf_{20}$ and $Nb_{30}Mo_{30}Co_{20}Zr_{20}$ become closer. The yield stress of the $Nb_{30}Mo_{30}Co_{20}Zr_{20}$ alloy is no-

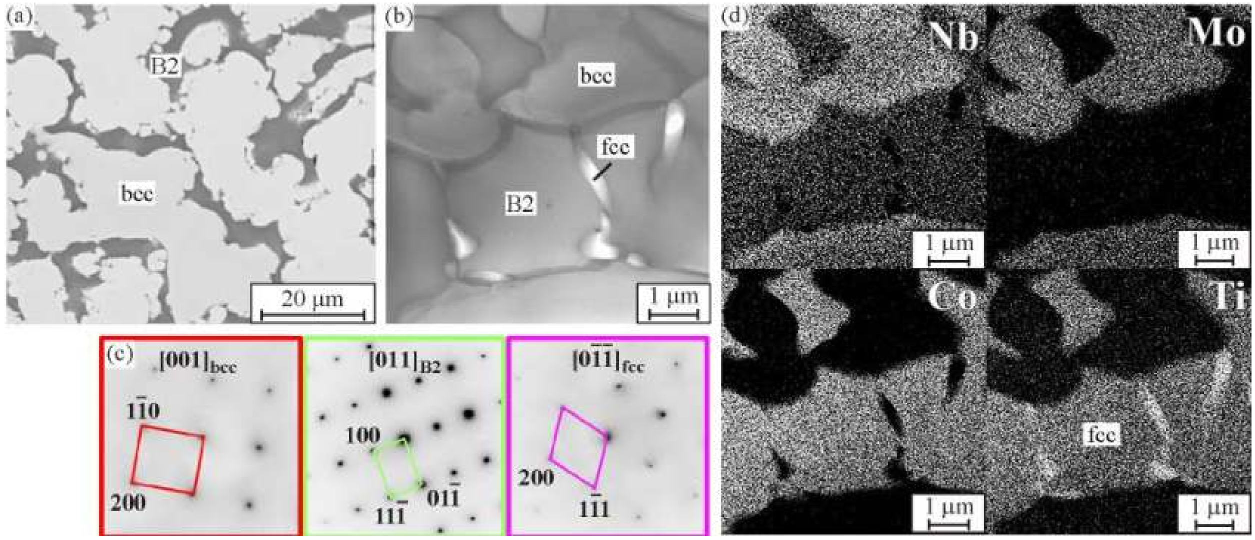

Fig. 3. Microstructure of the $Nb_{30}Mo_{30}Co_{20}Ti_{20}$ alloy: SEM image (a); STEM image (b); SAED patterns from the bcc, B2 and fcc phases (c); element distribution maps (d) (color online).

ticeably lower in the entire temperature range (Fig. 4, Table 3). The replacement of Hf by Ti leads to a certain increase in the strength at the temperatures 800 and 1000°C (Figs. 4c, 4d, Table 3). At the same time, the strain to fracture of the $Nb_{30}Mo_{30}Co_{20}Ti_{20}$ alloy in the temperature range 22–800°C does not exceed 30% and is the lowest among the studied alloys (Figs. 4a–4c,Table 3). Moreover, all the studied alloys are characterized by an unusually high strain hardening at temperatures up to 800°C (Figs. 4a–4c).

3.3. Microstructure after Testing for Uniaxial Compression

When tested for room-temperature uniaxial compression (Fig. 5a), the $Nb_{30}Mo_{30}Co_{20}Hf_{20}$ alloy re-

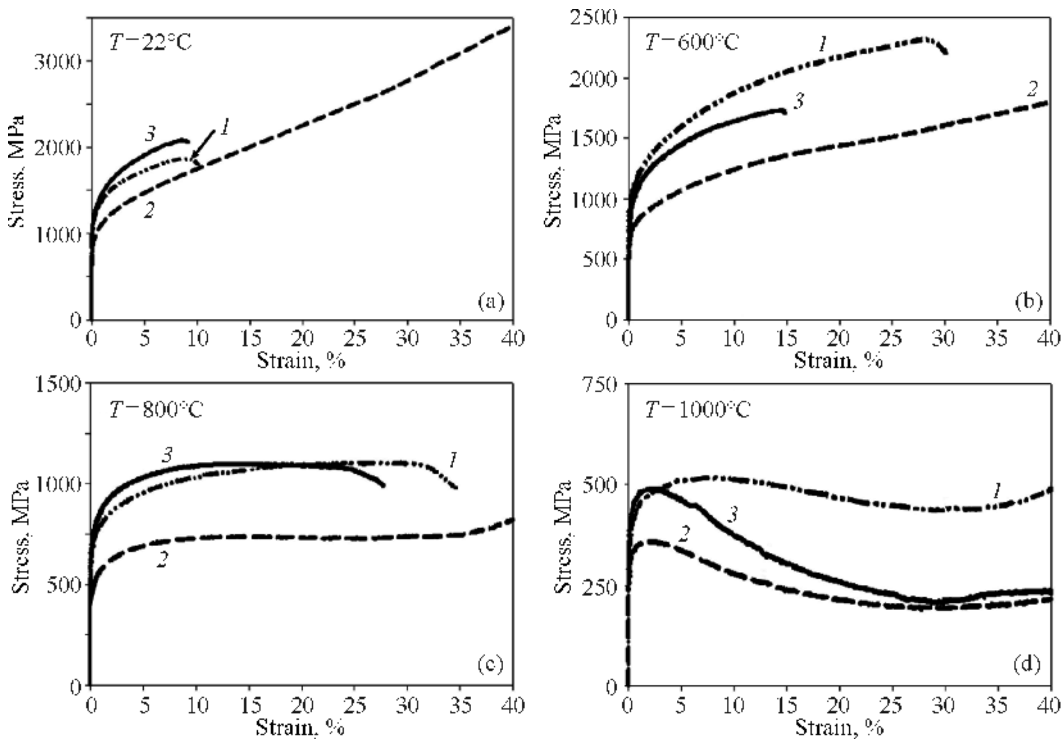

Fig. 4. Stress–strain curves of the alloys $Nb_{30}Mo_{30}Co_{20}Hf_{20}$ (*1*), $Nb_{30}Mo_{30}Co_{20}Zr_{20}$ (*2*), and $Nb_{30}Mo_{30}Co_{20}Ti_{20}$ (*3*) obtained during uniaxial compression tests at the temperatures 22 (a), 600 (b), 800 (c), and 1000°C (d).

Table 3. Mechanical properties of the alloys $Nb_{30}Mo_{30}Co_{20}Hf_{20}$, $Nb_{30}Mo_{30}Co_{20}Zr_{20}$, and $Nb_{30}Mo_{30}Co_{20}Ti_{20}$ ($\sigma_{0.2}$—yield strength, σ_{peak}—peak stress, ε_{peak}—strain at the peak stress, ε—fracture strain) after uniaxial compression at the temperature 22–1000°C

Alloy	Temperature, °C	$\sigma_{0.2}$, MPa	σ_{peak}, MPa	ε_{peak}, %	ε, %
$Nb_{30}Mo_{30}Co_{20}Hf_{20}$	22	1180 ± 75	1865 ± 80	8.8 ± 0.3	10.0 ± 0.5
	600	1000 ± 90	2325 ± 75	28.0 ± 0.8	30.0 ± 0.8
	800	685 ± 65	1105 ± 35	27.2 ± 0.9	35.0 ± 0.3
	1000	370 ± 40	520 ± 20	4.6 ± 0.4	>40.0
$Nb_{30}Mo_{30}Co_{20}Zr_{20}$	22	910 ± 40	3410 ± 60	37.0 ± 0.3	>40.0
	600	705 ± 55	1645 ± 55	32.3 ± 1.3	>40.0
	800	470 ± 30	742 ± 40	15.6 ± 0.8	>40.0
	1000	325 ± 35	360 ± 25	2.2 ± 0.1	>40.0
$Nb_{30}Mo_{30}Co_{20}Ti_{20}$	22	1185 ± 80	2075 ± 65	8.5 ± 0.6	9.0 ± 0.4
	600	900 ± 60	1735 ± 40	14.6 ± 0.4	15.1 ± 0.1
	800	740 ± 75	1100 ± 35	16.8 ± 0.2	27.8 ± 0.4
	1000	415 ± 35	490 ± 35	2.5 ± 0.1	>40

veals cracks that propagate mainly in the bcc phase and change direction when they meet the B2 particles. The bcc particles and the B2 phase exhibit an inhomogeneous contrast, which is probably due to the formation of the dislocation substructure. At 600°C (Fig. 5b), the crack growth behavior is the same: cracks form in the bcc phase, often change their direction at the phase boundary and do not propagate in the B2 phase. Strain contrast is also observed within the phases. After uniaxial compression at 800°C (Fig. 5c), the microstructure is different. There occur deformation localization and shear band formation. Cracks propagate mainly at the bcc-B2 phase boundary. The bcc particles are seen to elongate in the direction of plastic flow (indicated by an arrow in Fig. 5c). At 1000°C, no cracks are visible (Fig. 5d), but pores are pronounced at the bcc-B2 phase boundary. Fine particles form in the B2 phase. The bcc particles also appear to elongate in the plastic flow direction.

After uniaxial compression in the temperature range 22–1000°C, the $Nb_{30}Mo_{30}Co_{20}Zr_{20}$ alloy exhibits no cracks, but pores form in the B2 phase (Figs. 6a, 6b). Increasing the test temperature increases the number and size of pores. In the entire temperature range, bcc particles become flattened and elongated in the plastic flow direction. At the temperature 1000°C, similarly to the $Nb_{30}Mo_{30}Co_{20}Hf_{20}$ alloy

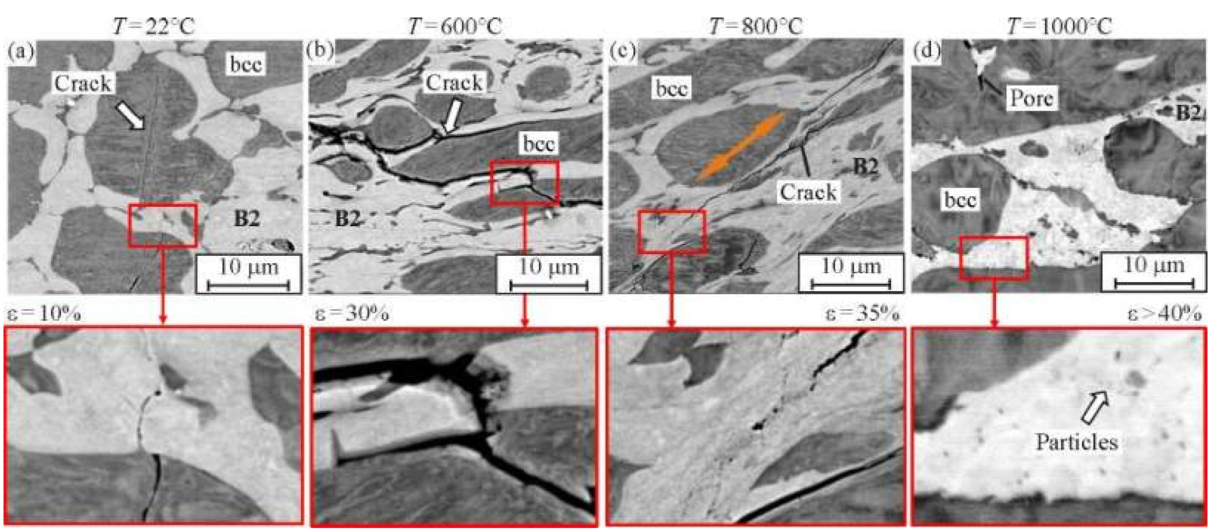

Fig. 5. Microstructure of the $Nb_{30}Mo_{30}Co_{20}Hf_{20}$ alloy after uniaxial compression tests at the temperatures 22 (a), 600 (b), 800 (c), and 1000°C (d) (color online).

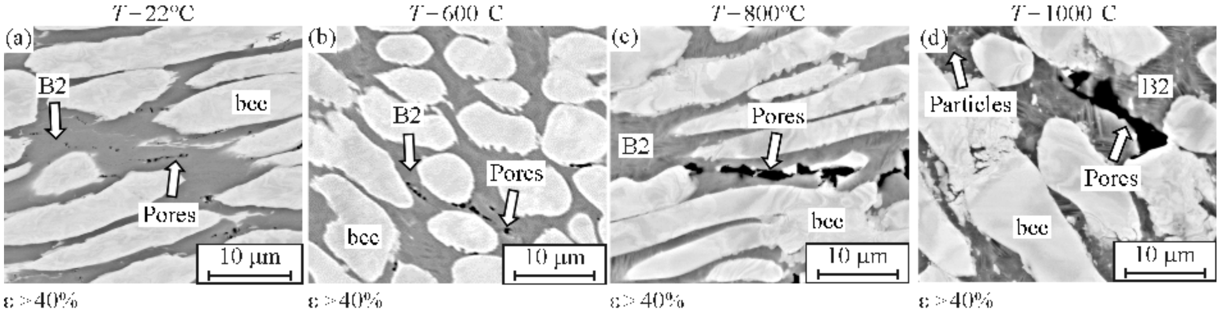

Fig. 6. Microstructure of the $Nb_{30}Mo_{30}Co_{20}Zr_{20}$ alloy after uniaxial compression tests at the temperatures 22 (a), 600 (b), 800 (c), and 1000°C (d).

(Fig. 5d), numerous fine particles (of the average size 175 ± 72 nm) form in the B2 phase (Fig. 6d).

In the $Nb_{30}Mo_{30}Co_{20}Ti_{20}$ alloy, as in $Nb_{30}Mo_{30}Co_{20}Hf_{20}$, cracks are initiated in the bcc particles and retarded in the B2 phase with the change in their direction (Fig. 7). However, the bcc phase in the $Nb_{30}Mo_{30}Co_{20}Ti_{20}$ alloy remains brittle in the entire temperature range. In the range from 22 to 600°C, no signs of plastic deformation are detected in both phases. This suggests the apparent plasticity of the alloy in the stress–strain curves (Figs. 4a, 4b) because the relative strain increase is due to crack propagation. At the temperature 800–1000°C, the bcc and B2 phases show a strain contrast caused by the development of the dislocation substructure, which implies the plastic flow activation. At 1000°C, fine particles are precipitated in the B2 phase.

4. DISCUSSION

The experimental observations show that the alloys $Nb_{30}Mo_{30}Co_{20}Hf_{20}$, $Nb_{30}Mo_{30}Co_{20}Zr_{20}$, and $Nb_{30}Mo_{30}Co_{20}Ti_{20}$ have a similar microstructure consisting of the bcc and B2 phases. The phase composition of the alloys $Nb_{30}Mo_{30}Co_{20}Hf_{20}$, $Nb_{30}Mo_{30}Co_{20}Zr_{20}$, and $Nb_{30}Mo_{30}Co_{20}Ti_{20}$ was determined quite accurately using the CALPHAD method (CALculation of PHAse Diagrams). Figure 8a exhibits the phase diagram of the $Nb_{30}Mo_{30}Co_{20}Hf_{20}$ alloy. Thermodynamic modeling predicts the separation of the liquid phase into the (Nb, Mo)- and (Hf, Co)-rich phases, which crystallize into the bcc and B2 phases, respectively. Liquid phase separation is usually associated with a positive enthalpy of mixing (ΔH_{mix}) [35]. In this alloy, the elements Hf and Co have a high affinity, and the repelling interaction is found between the particles Nb and Hf, i.e. positive enthalpy of mixing (Table 4). Recent studies report that the separation can also be affected by negative enthalpy of mixing [37], so it is most likely that, in this case, both components influence the liquid phase separation.

Though the Thermo-Calc software does not predict the liquid phase separation in the $Nb_{30}Mo_{30}Co_{20}Zr_{20}$ and $Nb_{30}Mo_{30}Co_{20}Ti_{20}$ alloys (Figs. 8b, 8c), the enthalpy of mixing in the Nb–Zr and Nb–Ti pairs is also positive, as in the Nb–Hf pair (Table 4). Therefore, the possibility of liquid phase separation in these alloys cannot be excluded. In the $Nb_{30}Mo_{30}Co_{20}Zr_{20}$ (Fig. 8b) and $Nb_{30}Mo_{30}Co_{20}Ti_{20}$ (Fig. 8c) alloys, the solidus temperature is lower than that in the $Nb_{30}Mo_{30}Co_{20}Hf_{20}$ alloy (Fig. 8a). Thus, the melting point is 1620°C in the $Nb_{30}Mo_{30}Co_{20}Hf_{20}$ alloy,

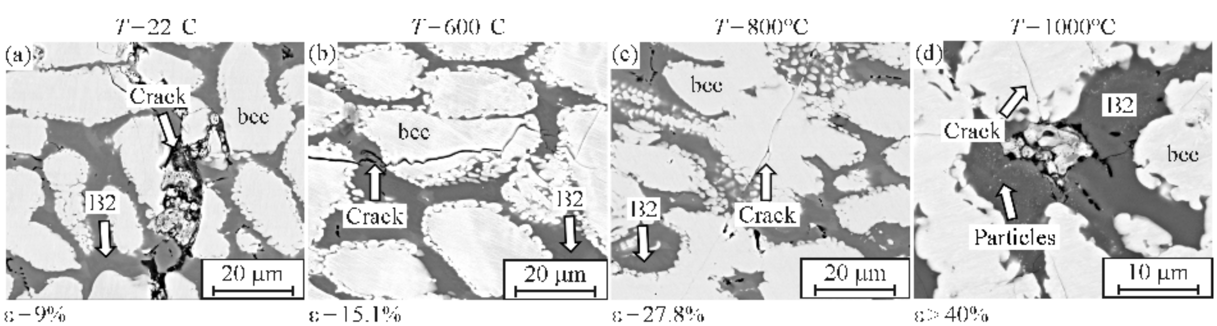

Fig. 7. Microstructure of the $Nb_{30}Mo_{30}Co_{20}Ti_{20}$ alloy after uniaxial compression tests at the temperatures 22 (a), 600 (b), 800 (c), and 1000°C (d).

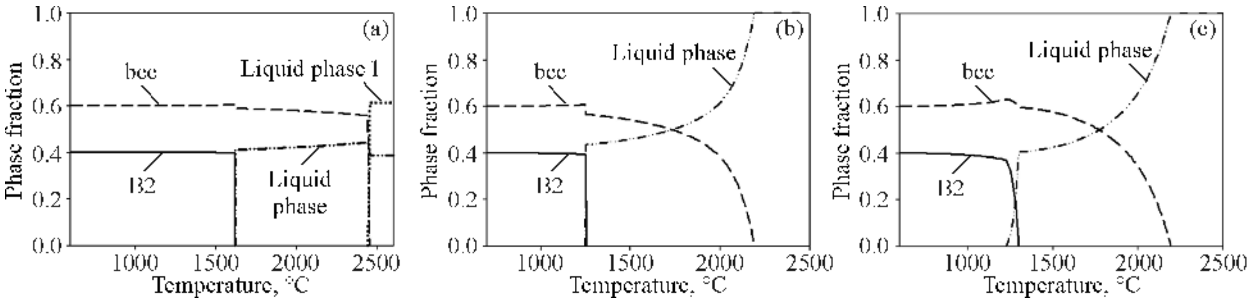

Fig. 8. Fraction of equilibrium phases as a function of the temperature for the $Nb_{30}Mo_{30}Co_{20}Hf_{20}$ (a), $Nb_{30}Mo_{30}Co_{20}Zr_{20}$ (b), and $Nb_{30}Mo_{30}Co_{20}Ti_{20}$ (c) alloys.

and it is 1250 and 1228°C in the $Nb_{30}Mo_{30}Co_{20}Zr_{20}$ and $Nb_{30}Mo_{30}Co_{20}Ti_{20}$ alloys, respectively.

According to thermodynamic modeling for the three alloys, the volume fractions of the bcc and B2 phases are 0.6 and 0.4, respectively. The experimental data suggest that the volume fraction of the phases is determined most accurately for the $Nb_{30}Mo_{30}Co_{20}Zr_{20}$ alloy (Fig. 8b, Table 2). The measured volume fraction of the bcc phase is 51.1% for the $Nb_{30}Mo_{30}Co_{20}Hf_{20}$ alloy, which is lower than the predicted value, and 70% for the $Nb_{30}Mo_{30}Co_{20}Ti_{20}$ alloy, which exceeds the predicted value (Figs. 8a, 8c, Table 2).

Despite the similar phase composition and phase morphology, the alloys show significant differences in mechanical properties. To gain a better understanding of the influence of each phase on the overall deformation behavior, we measured microhardness of the phases of each alloy (Table 5). The $Nb_{30}Mo_{30}Co_{20}Hf_{20}$ and $Nb_{30}Mo_{30}Co_{20}Zr_{20}$ alloys have similar microhardness values of both phases, however, the elastic modulus of the $Nb_{30}Mo_{30}Co_{20}Zr_{20}$ alloy is lower, which can explain its higher ductility at $T = 22$–800°C and noticeably lower strength (Fig. 4, Table 3). The highest hardness and elastic modulus are found for the bcc phase of the $Nb_{30}Mo_{30}Co_{20}Ti_{20}$ alloy, which makes it brittle even at 1000°C (Fig. 7d). In the previous study of the $Nb_{30}Mo_{30}Co_{20}Ti_{20}$ alloy [34], the brittleness of the bcc phase in this alloy was associated with oxygen-assisted embrittlement, while the heat treatment proposed in the paper increased the alloy ductility several times.

One of the parameters characterizing high-temperature alloys is the specific yield strength, which shows the ratio of strength to density of the alloy. At room temperature, the specific yield strength is 114, 106, and 144 MPa g/cm^3 for the alloys $Nb_{30}Mo_{30}Co_{20}Hf_{20}$, $Nb_{30}Mo_{30}Co_{20}Zr_{20}$, and $Nb_{30}Mo_{30}Co_{20}Ti_{20}$, respectively (Fig. 9a, Table 6). The $Nb_{30}Mo_{30}Co_{20}Hf_{20}$ and $Nb_{30}Mo_{30}Co_{20}Ti_{20}$ alloys demonstrate similar temperature dependences of the specific yield strength: at the temperature 1000°C, the specific yield strength is 35 and 50 MPa g/cm^3, respectively (alloys *1* and *3* in Fig. 9a). The $Nb_{30}Mo_{30}Co_{20}Zr_{20}$ alloy exhibits a noticeable decrease in the specific yield strength at 800°C. Increasing the test temperature to 1000°C does not decrease this characteristic: the specific yield strength is 35 MPa g/cm^3 at 800°C and 38 MPa g/cm^3 at 1000°C (alloy 2 in Fig. 9a). The highest specific yield strength is found for the $Nb_{30}Mo_{30}Co_{20}Ti_{20}$ alloy, which turns out to be higher than

Table 4. Enthalpy of mixing of the constituents [36] of the alloys $Nb_{30}Mo_{30}Co_{20}Hf_{20}$, $Nb_{30}Mo_{30}Co_{20}Ti_{20}$, and $Nb_{30}Mo_{30}Co_{20}Zr_{20}$

ΔH_{mix}, kJ/mol	Nb	Mo	Co	Hf	Zr	Ti
Nb	–	–5.7	–24.5	3.9	3.9	2.0
Mo	–	–	–4.9	–4.0	–6.2	–3.6
Co	–	–	–	–34.7	–40.3	–28.3
Hf	–	–	–	–	–0.2	0.2
Zr	–	–	–	–	–	–0.2
Ti	–	–	–	–	–	–

Table 5. Microhardness and elastic modulus of the bcc and B2 phases in the alloys $Nb_{30}Mo_{30}Co_{20}Hf_{20}$, $Nb_{30}Mo_{30}Co_{20}Ti_{20}$, and $Nb_{30}Mo_{30}Co_{20}Zr_{20}$

Alloy	Phase	Microhardness, GPa	E, GPa
$Nb_{30}Mo_{30}Co_{20}Hf_{20}$	B2	6.6 ± 0.7	214.1 ± 7.4
	bcc	7.5 ± 0.6	258.9 ± 6.3
$Nb_{30}Mo_{30}Co_{20}Zr_{20}$	B2	6.5 ± 0.3	177.0 ± 8.2
	bcc	7.2 ± 0.4	226.7 ± 4.9
$Nb_{30}Mo_{30}Co_{20}Ti_{20}$	B2	6.9 ± 0.4	200.8 ± 8.8
	bcc	9.2 ± 0.8	278.5 ± 5.9

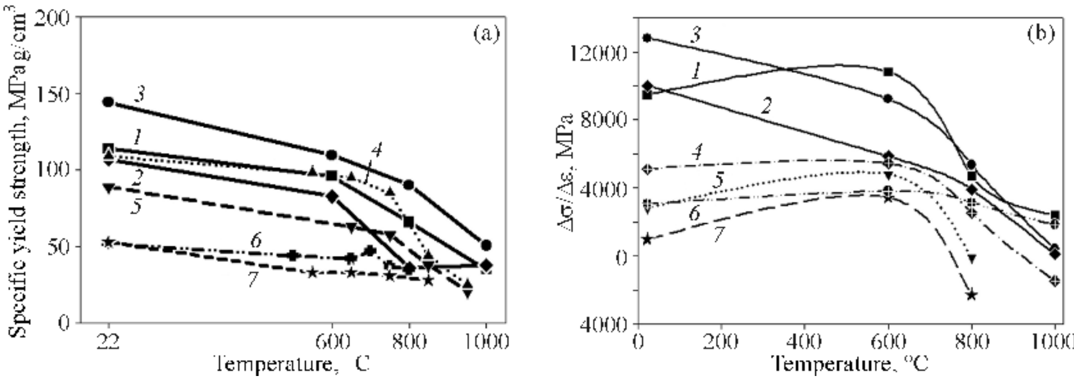

Fig. 9. Temperature dependence of specific yield strength (a): $Nb_{30}Mo_{30}Co_{20}Hf_{20}$ (*1*), $Nb_{30}Mo_{30}Co_{20}Zr_{20}$ (*2*), $Nb_{30}Mo_{30}Co_{20}Ti_{20}$ (*3*), Waspaloy [38] (*4*), Mar-M-302 [39] (*5*), Co-9Al- 9W [40] (*6*), and Haynes 188 [41] (*7*); temperature dependence of the strain hardening parameter Δσ/Δε (b): $Nb_{30}Mo_{30}Co_{20}Hf_{20}$ (*1*), $Nb_{30}Mo_{30}Co_{20}Zr_{20}$ (*2*), $Nb_{30}Mo_{30}Co_{20}Ti_{20}$ (*3*), HfNbTaTiZr [42] (*4*), $AlNbTiVZr_{0.5}$ [43] (*5*), C-3009 [44] (*6*), and $l_{0.5}CrNbTi_2V_{0.5}$ [45] (*7*).

that of hafnium and zirconium alloys, and also higher than the specific strength values presented in Fig. 9a for commercial alloys, such as Waspaloy, Mar-M-302, Co-9Al-9W, and Haynes 188. The specific ultimate strength of the zirconium alloy at 22–800°C is found to be lower than that of the hafnium alloy, but, at 1000°C, the alloys show similar values of specific strength. The specific characteristics of both alloys at 1000°C are higher than those of commercial nickel-based Waspaloy superalloy used for parts of gas turbine engines, springs and fasteners, as well as of the presented nickel and cobalt superalloys.

Table 6. Specific yield strength and strain hardening of the alloys $Nb_{30}Mo_{30}Co_{20}Hf_{20}$, $Nb_{30}Mo_{30}Co_{20}Zr_{20}$, and $Nb_{30}Mo_{30}Co_{20}Ti_{20}$

Alloy	Temperature, °C	Specific yield strength, MPa g/cm^3	Δσ/Δε, MPa
$Nb_{30}Mo_{30}Co_{20}Hf_{20}$	22	114 ± 5	9479 ± 155
	600	96 ± 3	10 833 ± 130
	800	66 ± 4	4688 ± 115
	1000	35 ± 3	2396 ± 95
$Nb_{30}Mo_{30}Co_{20}Zr_{20}$	22	106 ± 4	10 000 ± 105
	600	82 ± 5	5854 ± 75
	800	35 ± 3	3916 ± 60
	1000	38 ± 2	125 ± 65
$Nb_{30}Mo_{30}Co_{20}Ti_{20}$	22	144 ± 4	12 812 ± 125
	600	109 ± 3	9229 ± 110
	800	90 ± 3	5354 ± 85
	1000	50 ± 2	416 ± 65

In addition, the alloys under consideration are highly prone to strain hardening, which is not typical for multiphase refractory high-entropy alloys [43, 45–49]. The temperature dependence of strain hardening is calculated by the formula $\Delta\sigma/\Delta\varepsilon = (\sigma_{0.05} - \sigma_{0.002})/(0.05 - 0.002)$ [31], which shows the rate of change in strain hardening between the true strain $\varepsilon = 0.05$ and yield strength ($\varepsilon = 0.002$) (Fig. 9b, Table 6). The used range seems suitable for comparing the post-yield behavior of different HEA and other refractory alloys in terms of room-temperature ductility and resistance to softening at high temperatures. The $Nb_{30}Mo_{30}Co_{20}Hf_{20}$ alloy, like the $Nb_{30}Mo_{30}Co_{20}Ti_{20}$ alloy, shows high Δσ/Δε values (~10 000 MPa) in the range of 22–600°C compared to the studied analogues. However, when approaching $T = 800$–1000°C, the parameter Δσ/Δε of the alloys decreases noticeably, but is still superior to all multiphase HEAs and the S-3009 alloy. The $Nb_{30}Mo_{30}Co_{20}Zr_{20}$ alloy has high Δσ/Δε values (~10 000 MPa) at room temperature, which however decrease significantly with increasing temperature, being lower than those of the $Nb_{30}Mo_{30}Co_{20}Hf_{20}$ and $Nb_{30}Mo_{30}Co_{20}Ti_{20}$.

5. CONCLUSIONS

The structure and mechanical properties were studied and compared for high-entropy alloys $Nb_{30}Mo_{30}Co_{20}Hf_{20}$, $Nb_{30}Mo_{30}Co_{20}Ti_{20}$, and $Nb_{30}Mo_{30}Co_{20}Zr_{20}$ with a bcc + B2 structure.

The alloys $Nb_{30}Mo_{30}Co_{20}Hf_{20}$, $Nb_{30}Mo_{30}Co_{20}Ti_{20}$, and $Nb_{30}Mo_{30}Co_{20}Zr_{20}$ had a similar phase composition. The alloys consisted of a Co- and Hf/Zr/Ti-rich B2 matrix and (Nb, Mo)-rich bcc particles. A small volume fraction of Nb-rich particles (≤1.5%) was detected in the $Nb_{30}Mo_{30}Co_{20}Hf_{20}$ and $Nb_{30}Mo_{30}Co_{20}Zr_{20}$ alloys. Titanium oxides (TiO_2) (≤1%) were found in the $Nb_{30}Mo_{30}Co_{20}Ti_{20}$ alloy.

The $Nb_{30}Mo_{30}Co_{20}Ti_{20}$ alloy had the highest yield strength, and the $Nb_{30}Mo_{30}Co_{20}Zr_{20}$ alloy was the most ductile. $Nb_{30}Mo_{30}Co_{20}Hf_{20}$ showed the most balanced properties in the range of 22–1000°C. All alloys demonstrated high strain hardening in the temperature range 22–800°C.

The specific yield strength of the $Nb_{30}Mo_{30}Co_{20}Ti_{20}$ alloy exceeded that of $Nb_{30}Mo_{30}Co_{20}Hf_{20}$ and $Nb_{30}Mo_{30}Co_{20}Zr_{20}$ and also the specific strength of commercial heat-resistant alloys Waspaloy, Mar-M-302, Co-9Al-9W, and Haynes 188.

The $Nb_{30}Mo_{30}Co_{20}Hf_{20}$ and $Nb_{30}Mo_{30}Co_{20}Ti_{20}$ alloys showed a higher rate of strain hardening in the temperature range 22–600°C compared to other refractory high-entropy alloys. The $Nb_{30}Mo_{30}Co_{20}Zr_{20}$ alloy demonstrated a high rate of strain hardening at room temperature, which, however, decreased significantly with increasing temperature and was lower than those of the $Nb_{30}Mo_{30}Co_{20}Hf_{20}$ and $Nb_{30}Mo_{30}Co_{20}Ti_{20}$ alloys.

FUNDING

The work was financially supported by Russian Science Foundation project No. 21-79-10043 (https://rscf.ru/project/21-79-10043/). The work was carried out using the equipment of the Technologies and Materials CUC of the Belgorod State University funded by the Ministry of Higher Education and Science of the Russian Federation under agreement No. 075-15-2021-690 (project identifier RF 2296.61321X0030).

CONFLICT OF INTEREST

The authors of this work declare that they have no conflicts of interest.

REFERENCES

1. Kracke, A., Superalloys, the Most Successful Alloy System of Modern Times—Past, Present, and Future, *TMS*, 2010, pp. 13–50. https://doi.org/10.7449/2010/superalloys_2010_13_50
2. Liu, L., Zhang, J., and Ai, C., Nickel-Based Superalloys, *Encycl. Mater. Met. Alloy.*, 2021, pp. 294–304. https://doi.org/10.1016/B978-0-12-803581-8.12093-4
3. Pineau, A. and Antolovich, S.D., High Temperature Fatigue of Nickel-Base Superalloys—A Review with Special Emphasis on Deformation Modes and Oxidation, *Eng. Fail. Anal.*, 2009, vol. 16, pp. 2668–2697. https://doi.org/10.1016/j.engfailanal.2009.01.010
4. Joseph, C., Persson, C., and Hörnqvist Colliander M., Influence of Heat Treatment on the Microstructure and Tensile Properties of Ni-Base Superalloy Haynes 282, *Mater. Sci. Eng. A*, 2017, vol. 679, pp. 520–530. https://doi.org/10.1016/j.msea.2016.10.048
5. Zenk, C.H., Neumeier, S., Engl, N.M., Fries, S.G., Dolotko, O., Weiser, M., Virtanen, S., and Göken, M., Intermediate Co/Ni-Base Model Superalloys—Thermophysical Properties, Creep and Oxidation, *Scripta Mater.*, 2016, vol. 112, pp. 83–86. https://doi.org/10.1016/j.scriptamat.2015.09.018
6. Ruzic, J., Goto, K., Watanabe, I., Osada, T., Wu, L., and Ohmura, T., Temperature-Dependent Deformation Behavior of γ and γ′ Single-Phase Nickel-Based Superalloys, *Mater. Sci. Eng. A*, 2021, vol. 818, p. 141439. https://doi.org/10.1016/j.msea.2021.141439
7. Osada, T., Gu, Y., Nagashima, N., Yuan, Y., Yokokawa, T., and Harada, H., Optimum Microstructure Combination for Maximizing Tensile Strength in a Polycrystalline Superalloy with a Two-Phase Structure, *Acta Mater.*, 2013, vol. 61, pp. 1820–1829. https://doi.org/10.1016/j.actamat.2012.12.004
8. Osada, T., Nagashima, N., Gu, Y., Yuan, Y., Yokokawa, T., and Harada, H., Factors Contributing to the Strength of a Polycrystalline Nickel-Cobalt Base Superalloy, *Scripta Mater.*, 2011, vol. 64, pp. 892–895. https://doi.org/10.1016/j.scriptamat.2011.01.027
9. Perepezko, J.H., The Hotter the Engine, the Better, *Science*, 2009, vol. 326, pp. 1068–1069. https://doi.org/10.1126/science.1179327
10. Senkov, O.N., Miracle, D.B., Chaput, K.J., and Couzinie, J.P., Development and Exploration of Refractory High Entropy Alloys—A Review, *J. Mater. Res.*, 2018, vol. 33, pp. 3092–3128. https://doi.org/10.1557/jmr.2018.153
11. Tsai, M.H. and Yeh, J.W., High-Entropy Alloys: A Critical Review, *Mater. Res. Lett.*, 2014, no. 2, pp. 107–123. https://doi.org/10.1080/21663831.2014.912690
12. George, E.P., Raabe, D., and Ritchie, R.O., High-Entropy Alloys, *Nat. Rev. Mater.*, 2019, no. 4, pp. 515–534. https://doi.org/10.1038/s41578-019-0121-4
13. Miracle, D.B. and Senkov, O.N., A Critical Review of High Entropy Alloys and Related Concepts, *Acta Mater.*, 2017, vol. 122, pp. 448–511. https://doi.org/10.1016/j.actamat.2016.08.081
14. Zhang, Y., Zuo, T.T., Tang, Z., Gao, M.C., Dahmen, K.A., Liaw, P.K., and Lu, Zh.P., Microstructures

and Properties of High-Entropy Alloys, *Prog. Mater. Sci*., 2014, vol. 61, pp. 1–93. https://doi.org/10.1016/j.pmatsci.2013.10.001

15. Liu, X.W., Bai, Z.C., Ding, X.F., Yao, J.Q., Wang, L., Su, Y.Q., Fan, Z.T., and Guo, J.J., A Novel Light-Weight Refractory High-Entropy Alloy with High Specific Strength and Intrinsic Deformability, *Mater. Lett*., 2021, vol. 287, pp. 129255. https://doi.org/10.1016/j.matlet.2020.129255
16. Juan, C.C., Tsai, M.H., Tsai, C.W., Lin, C.M., Wang, W.R., Yang, C.C., Chen, S.K., Lin, S.J., and Yeh, J.W., Enhanced Mechanical Properties of HfMoTaTiZr and HfMoNbTaTiZr Refractory High-Entropy Alloys, *Intermetallics*, 2015, vol. 62, pp. 76–83. https://doi.org/10.1016/j.intermet.2015.03.01
17. Senkov, O.N., Isheim, D., Seidman, D.N., and Pilchak, A.L., Development of a Refractory High Entropy Superalloy, *Entropy*, 2016, vol. 18, p. 102. https://doi.org/10.3390/E18030102
18. Wu, Y.D., Cai, Y.H., Wang, T., Si, J.J., Zhu, J., Wang, Y.D., and Hui, X.D., A Refractory $Hf_{25}Nb_{25}Ti_{25}Zr_{25}$ High-Entropy Alloy with Excellent Structural Stability and Tensile Properties, *Mater. Lett*., 2014, vol. 130, pp. 277–280. https://doi.org/10.1016/j.matlet.2014.05.134
19. Senkov, O.N., Wilks, G.B., Miracle, D.B., Chuang, C.P., and Liaw, P.K., Refractory High-Entropy Alloys, *Intermetallics*, 2010, vol. 18, pp. 1758–1765. https://doi.org/10.1016/j.intermet.2010.05.014
20. Reed, R.C., *The Superalloys Fundamentals and Applications*, Cambridge: Cambridge University Press, 2006. https://doi.org/10.1017/CBO9780511541285
21. Senkov, O.N., Senkova, S.V., and Woodward, C., Effect of Aluminum on the Microstructure and Properties of Two Refractory High-Entropy Alloys, *Acta Mater*., 2014, vol. 68, pp. 214–228. https://doi.org/10.1016/j.actamat.2014.01.029
22. Miracle, D.B., Tsai, M.H., Senkov, O.N., Soni, V., and Banerjee, R., Refractory High Entropy Superalloys (RSAs), *Scripta Mater*., 2020, vol. 187, pp. 445–452. https://doi.org/10.1016/j.scriptamat.2020.06.048
23. Whitfield, T.E., Pickering, E.J., Owen, L.R., Jones, C.N., Stone, H.Y., and Jones, N.G., The Effect of Al on the Formation and Stability of a BCC–B2 Microstructure in a Refractory Metal High Entropy Superalloy System, *Materialia*, 2020, vol. 13, p. 100858. https://doi.org/10.1016/j.mtla.2020.100858
24. Cao, B.X., Yang, T., Fan, L., Luan, J.H., Jiao, Z.B., and Liu, C.T., Refractory Alloying Additions on the Thermal Stability and Mechanical Properties of High-Entropy Alloys, *Mater. Sci. Eng. A*, 2020, vol. 797, p. 140020. https://doi.org/10.1016/j.msea.2020.140020
25. Soni, V., Gwalani, B., Alam, T., Dasari, S., Zheng, Y., Senkov, O.N., Miracle, D., and Banerjee, R., Phase Inversion in a Two-Phase, BCC + B2, Refractory High Entropy Alloy, *Acta Mater*., 2020, vol. 185, pp. 89–97. https://doi.org/10.1016/j.actamat.2019.12.004
26. Soni, V., Gwalani, B., Senkov, O.N., Viswanathan, B., Alam, T., Miracle, D.B., and Banerjee, R., Phase Stability as a Function of Temperature in a Refractory High-Entropy Alloy, *J. Mater. Res*., 2018, vol. 33, pp. 3235–3246. https://doi.org/10.1557/jmr.2018.223
27. Oliver, W.C. and Pharr, G.M., Measurement of Hardness and Elastic Modulus by Instrumented Indentation: Advances in Understanding and Refinements to Methodology, *J. Mater. Res*., 2004, vol. 19, pp. 3–20. https://doi.org/10.1557/jmr.2004.19.1.3
28. Van Essen, R.M. and Buschow, K.H.J., Hydrogen Absorption in Various Zirconium- and Hafnium-Based Intermetallic Compounds, *J. Less Common Met*., 1979, vol. 64, pp. 277–284. https://doi.org/10.1016/0022-5088(79)90178-4
29. Hubbell, W.C. and Brotzen, F.R., Elastic Constants of Niobium-Molybdenum Alloys in the Temperature Range –190 to +100°C, *J. Appl. Phys*., 1972, vol. 43, pp. 3306–3312. https://doi.org/10.1063/1.1661712
30. Knowles, A.J., Dye, D., Dodds, R.J., Watson, A., Hardie, C.D., and Humphry-Baker, S.A., Tungsten-Based BCC-Superalloys, *Appl. Mater. Today*, 2021, vol. 23, p. 101014. https://doi.org/10.1016/j.apmt.2021.101014
31. Yurchenko, N., Panina, E., Shaysultanov, D., Zherebtsov, S., and Stepanov, N., Refractory High Entropy Alloy with Ductile Intermetallic B2 Matrix/Hard BCC Particles and Exceptional Strain Hardening Capacity, *Materialia*, 2021, vol. 20, p. 101225. https://doi.org/10.1016/j.mtla.2021.101225
32. Takasugi, M.Y.T. and Izumi, O., Anomalous Temperature Dependence of the Yield Strength in IVa-Vlll Intermetallic Compounds with B2 Structure, *J. Mater. Sci*., 1991, vol. 26, pp. 2941–2948. https://doi.org/10.1007/bf01124825
33. Wollmershauser, J.A., Neil, C.J., and Agnew, S.R., Mechanisms of Ductility in CoTi and CoZr B2 Intermetallics, *Metal. Mater. Trans A*, 2010, vol. 41, p. 1217. https://doi.org/10.1007/s11661-009-9990-2
34. Yurchenko, N., Panina, E., Rogal, Ł., Shekhawat, L., Zherebtsov, S., and Stepanov, N., Unique Precipitations in a Novel Refractory Nb-Mo-Ti-Co High-Entropy Superalloy, *Mater. Res. Lett*., 2022, vol. 10, pp. 78–87. https://doi.org/10.1080/21663831.2021.2022033
35. Nagase, T., Todai, M., and Nakano, T., Development of Ti–Zr–Hf–Y–La High-Entropy Alloys with Dual Hexagonal-Close-Packed Structure, *Scripta Mater*., 2020, vol. 186, pp. 242–246. https://doi.org/10.1016/j.scriptamat.2020.05.033
36. Takeuchi, A. and Inoue, A., Mixing Enthalpy of Liquid Phase Calculated by Miedema's Scheme and Approximated with Sub-Regular Solution Model for Assessing Forming Ability of Amorphous and Glassy Alloys, *Intermetallics*, 2010, vol. 18, pp. 1779–1789. https://doi.org/10.1016/j.intermet.2010.06.003
37. Munitz, A., Edry, I., Brosh, E., Derimow, N., MacDonald, B.E., Lavernia, E.J., and Abbaschian, R., Liquid Phase Separation in $AlCrFeNiMo_{0.3}$ High-Entropy Al-

loy, *Intermetallics*, 2019, vol. 112, p. 106517. https://doi.org/10.1016/j.intermet.2019.106517
38. Sims, C.T., Stoloff, N.S., and Hagel, W.C., *Superalloys II: High Temperature Materials for Aerospace and Industrial Power*, New York: Wiley Sons, 1987, vol. 208.
39. Kaufman, M., Properties of Cast MAR-M-247 for Turbine Blisk Applications, in *Superalloys: V Int. Symp*., 1984, pp. 43–52.
40. Suzuki, A., DeNolf, G.C., and Pollock, T.M., Flow Stress Anomalies in γ/γ' Two-Phase Co-Al-W-Base Alloys, *Scripta Mater*., 2007, vol. 56, pp. 385–388. https://doi.org/10.1016/j.scriptamat.2006.10.039
41. Lee, W.S. and Kao, H.C., High Temperature Deformation Behaviour of Haynes 188 Alloy Subjected to High Strain Rate Loading, *Mater. Sci. Eng. A*, 2014, vol. 594, pp. 292–301. https://doi.org/10.1016/j.msea.2013.11.076
42. Senkov, O.N., Scott, J.M., Senkova, S.V., Meisenkothen, F., Miracle, D.B., and Woodward, C.F., Microstructure and Elevated Temperature Properties of a Refractory TaNbHfZrTi Alloy, *J. Mater. Sci*., 2012, vol. 47, pp. 4062–4074. https://doi.org/10.1007/s10853-012-6260-2
43. Yurchenko, N.Y., Stepanov, N.D., Zherebtsov, S.V., Tikhonovsky, M.A., and Salishchev, G.A., Structure and Mechanical Properties of B2 Ordered Refractory $AlNbTiVZr_x$ ($x = 0$–1.5) High-Entropy Alloys, *Mater. Sci. Eng. A*, 2017, vol. 704, pp. 82–90. https://doi.org/10.1016/j.msea.2017.08.019
44. Senkov, O.N., Rao, S.I., Butler, T.M., Daboiku, T.I., and Chaput, K.J., Microstructure and Properties of Nb-Mo-Zr Based Refractory Alloys, *Int. J. Refract. Met. Hard Mater*., 2020, vol. 92, p. 105321. https://doi.org/10.1016/j.ijrmhm.2020.105321
45. Stepanov, N.D., Yurchenko, N.Y., Panina, E.S., Tikhonovsky, M.A., and Zherebtsov, S.V., Precipitation-Strengthened Refractory $Al_{0.5}CrNbTi_2V_{0.5}$ High Entropy Alloy, *Mater. Lett*., 2017, vol. 188, pp. 162–164. https://doi.org/10.1016/j.matlet.2016.11.030
46. Senkov, O.N., Jensen, J.K., Pilchak, A.L., Miracle, D.B., and Fraser, H.L., Compositional Variation Effects on the Microstructure and Properties of a Refractory High-Entropy Superalloy $AlMo_{0.5}NbTa_{0.5}TiZr$, *Mater. Des*., 2018, vol. 139, pp. 498–511. https://doi.org/10.1016/j.matdes.2017.11.033
47. Senkov, O.N., Couzinie, J.P., Rao, S.I., Soni, V., and Banerjee, R., Temperature Dependent Deformation Behavior and Strengthening Mechanisms in a Low Density Refractory High Entropy Alloy $Al_{10}Nb_{15}Ta_5Ti_{30}Zr_{40}$, *Materialia*, 2020, vol. 9, p. 100627. https://doi.org/10.1016/j.mtla.2020.100627
48. Senkov, O.N., Woodward, C., and Miracle, D.B., Microstructure and Properties of Aluminum-Containing Refractory High-Entropy Alloys, *JOM*, 2014, vol. 66, pp. 2030–2042. https://doi.org/10.1007/s11837-014-1066-0
49. Stepanov, N.D., Yurchenko, N.Y., Skibin, D.V., Tikhonovsky, M.A., and Salishchev, G.A., Structure and Mechanical Properties of the $AlCr_xNbTiV$ ($x = 0$, 0.5, 1, 1.5) High Entropy Alloys, *J. Alloys Compd*, 2015, vol. 652, pp. 266–280. https://doi.org/10.1016/j.jallcom.2015.08.224